Journal of Alloys and Compounds 804 (2019) 527–537

Contents lists available at ScienceDirect

Journal of Alloys and Compounds

journal homepage: http://www.elsevier.com/locate/jalcom

Studies of Zr-based C15 type metal hydride battery anode alloys prepared by rapid solidification

Ika Dewi Wijayanti [a, b, c, **], Live Mølmen [b], Roman V. Denys [a], Jean Nei [d], Stéphane Gorsse [e], Matylda N. Guzik [f], Kwo Young [d], Volodymyr Yartys [a, b, *]

[a] Department of Battery Technology, Institute for Energy Technology (IFE), Kjeller, Norway
[b] Department of Materials Science and Engineering, NTNU, Trondheim, Norway
[c] Department of Mechanical Engineering, ITS, Surabaya, Indonesia
[d] BASF/Battery Materials-Ovonic, Rochester Hills, USA
[e] Univ. Bordeaux, CNRS, Bordeaux INP, ICMCB, UMR 5026, Pessac F, 33600, France
[f] Department of Physics, University of Oslo, Blindern, Oslo, Norway

ARTICLE INFO

Article history:
Received 6 May 2019
Received in revised form
25 June 2019
Accepted 26 June 2019
Available online 27 June 2019

Keywords:
Ti-Zr alloys
Laves phase intermetallic
Rapid solidification
Metal hydride electrode
Electrochemical performance
EIS characterization

ABSTRACT

The objective of the present work was to study an interrelation between the conditions of the rapid solidification casting and electrochemical properties of a C15 Laves-type Zr-based metal hydride battery anode alloy. A 7-component overstoichiometric with B/A>2 alloy (Ni + Mn + V + Fe/Zr + Ti + La = 2.078) was Zr- and Ni-rich. Melt spinning was performed using as cast mother ingot at different rotation speeds of 5, 16.5, and 33 Hz with a 20-cm diameter Cu cooling wheel. The phase composition and morphology of the ribbons were analyzed by X-ray diffraction (XRD) and scanning electron microscopy (SEM) along with X-ray energy dispersive spectroscopy (EDS). Partial Mn vaporization took place during the melt spinning and became more pronounced with the increase in the quenching rate at higher wheel rotation speeds. The SEM study showed a successful refinement and a more homogeneous distribution of La in the melt-spun alloys. However, the alloys demonstrated a more difficult activation performance as compared to the as-cast sample which was associated with introduction of Zr into the composition of the secondary La-and Ni-rich phase when quenching the melt. Presence of Zr in the secondary phase results in inferior rate of its hydrogenation. The formed during the rapid solidification (La,Zr) (Ni,Mn) secondary phase also contained a significant amount of oxygen additionally worsening the activation performance. The grain size gradually decreased from 3.5 μm in the as-cast alloy to approximately 250 nm for the melt spun sample obtained at the highest cooling rate. The two-phase alloys contained a mixture of two Laves type intermetallics, C15 and C14 ones. The abundance of the secondary C14 phase decreased with increase of the cooling rate as compared to the as-cast sample. The electrochemical performance was significantly affected by the compositional and microstructural changes associated with the variation in the cooling rate. The highest electrochemical discharge capacity of 414 mAh/g was obtained for the 16.5 Hz melt spun rate because of an optimized composition of the Laves phase. Furthermore, the diffusion coefficient of hydrogen in this alloy was the highest in a full state of charge, which indicates that faster hydrogen diffusion and shorter hydrogen diffusion paths were achieved via an application of the rapid solidification process. An optimization of the rapid solidification conditions is required to improve an activation behavior of the studied Laves types metal hydride anode alloys.

1. Introduction

Intermetallic compounds which contain hydride-forming and transition metals can reversibly absorb large amounts of hydrogen to form intermetallic hydrides. The very first examples of such hydrides - rather stable ZrNiH and $ZrNiH_3$ formed by ZrNi

* Corresponding author. Institute for Energy Technology (IFE), Kjeller, Norway.
** Corresponding author. Institute for Energy Technology (IFE), Kjeller, Norway.
E-mail addresses: Ika.Dewi.Wijayanti@ife.no (I.D. Wijayanti), Volodymyr.Yartys@ife.no (V. Yartys).

https://doi.org/10.1016/j.jallcom.2019.06.324

intermetallic compound - have been reported already in the 1950s [1]. Increased relative amount of transition metal as in $LaNi_5$, destabilizes corresponding $LaNi_5H_{6.7}$ hydride (P_{abs}/P_{des} @20 °C of 1.83/1.36 atm H_2) [2]. As its equilibrium hydrogen pressure becomes close to 1 bar, this allows to synthesize it both by a reaction of intermetallic alloy with hydrogen gas but also electrochemically using the alloys as an anode electrode of the metal hydride battery. In spite of a high theoretical electrochemical capacity of 400 mAh/g, the instability of $LaNi_5$-based hydride at normal conditions results in its much lower capacity of around 250 mAh/g as compared to the theoretical limit [3]. Substitution of a part of Ni by Cr or Mn in $LaNi_{4.5}(Cr/Mn)_{0.5}$ increased reversible capacity by 10% to the values 275–285 mAh/g as the formed hydrides have dissociation pressures below 1 bar H_2. In practical applications a severe corrosion of $LaNi_5$ in the aqueous KOH electrolyte has been observed and this issue should be conteracted by modifying the alloy to make it suitable for applications in rechargeable batteries.

Optimum performance of the Nickel Metal Hydride (NiMH) batteries can be achieved by optimizing microstructure, type of intermetallic compound, constituting elements type and content, by changing the composition of hydrogen storage alloy (multicomponent alloy) or by adding electrocatalytic materials for facilitating the hydrogen evolution reaction [4]. As an example, excellent stability was achieved with a very small capacity loss of only 30% over one thousand cycles for $La_{0.8}Nd_{0.2}Ni_{2.5}Co_{2.4}Si_{0.1}$ alloy synthesized via a modification of $LaNi_5$. However, the high cost of rare-earth metals becomes the big challenge to utilize such type of alloys.

The discharge process of the metal hydride battery consisting of nickel hydroxide as a cathode, $LaNi_5$ as anode and aqueous solution of KOH as an electrolyte, has been successfully modelled by considering the electrochemical processes in porous electrodes with hydrogen diffusion coefficient in the $LaNi_5$ electrode being close to 5×10^{-11} cm^2/s [5]. This allowed to assess operating characteristics of the cell, while an optimization of the electrode thickness and the porosity was performed by considering the specific energy and power of the cell.

In order to improve the discharge efficiency and electrochemical properties, multicomponent AB_2 Laves phase alloys become the preference anode materials in the NiMH batteries as they exhibit higher discharge capacities than AB_5-type alloys, further to the Mg-containing $A_{3-x}Mg_xNi_9$ and $A_{2-x}Mg_xNi_7$ compositions [4,6]. Anani and his coworkers [7] reported that a multiphase $Ti_{0.51}Zr_{0.49}V_{0.76}Ni_{1.18}Cr_{0.21}$ alloy with a plateau pressure of 0.83 bar H_2 at ambient conditions, achieved a discharge capacity of 350 mAh/g, which was superior to the electrochemical performance of $LaNi_5$. Similar values of the capacity (350 mAh/g discharge capacity at 50 mA/g current density) were also reported for a multiphase $Zr_{0.8}Ti_{0.2}V_{0.6}Mn_{0.3}Ni_{0.9}Fe_{0.2}$ alloy [4].

The used Laves type intermetallic alloys belong to the largest group of the hydride-forming intermetallics and are utilized for storage of gaseous hydrogen and for the electrochemical storage in the metal hydride batteries. The structures of Laves phases contain a stacking of the layers with compositions A_2B, AB_2 and B_3. Variation of their stacking order results in the formation of different types of the Laves type intermetallics. The most promising Laves phase alloys that absorb hydrogen to form hydrides crystallize with hexagonal $MgZn_2$ (C14), cubic $MgCu_2$ (C15), and di-hexagonal $MgNi_2$ (C36) type structures [8]. For the metal hydride-based hydrogen storage applications, the most frequently utilized are the alloys with C14 and C15 types [9].

Hydrogen storage performance including hydrogen storage capacity, stability of the hydrides, kinetics of hydrogen absorption, and cycling performance are highly dependent on the type of Laves phase present in the alloys [10]. C15 type alloys exhibit excellent high-rate dischargeability (HRD) and are easier to activate than C14 type alloys [8,10,11]. To optimize and to improve the performance of the C15 predominate alloy, one approach is to perform substitutions in the parent alloy containing the transition elements [12,13]. Synthesis of non-stoichiometric alloys with $B/A \neq 2$ is frequently used to modify the properties via a multi-component alloying [14]. By combining certain elements (A = Ti, Zr, V; B= Mn, V, Ni, and Fe) to move the stoichiometry off with B/A becoming higher than 2, higher storage capacities, improved cycle life, and easier activation can be achieved [15]. Various participating elements have their own role in influencing the H storage performance. Hydride-forming A elements include Ti, Zr and V, while transition elements B have several functions, including increased catalytic activity in reduction-oxidation of hydrogen (Ni), improved surface activity to achieve fast hydrogen reduction or oxidation (Mn), and increased corrosion resistance (Fe). In addition to this conventional alloying strategy, it is worth to note that the present alloy satisfies the high entropy alloys definition [16–18], which consists in an entropy stabilization when mixing several kinds of atoms on the same sublattice.

Our earlier work revealed that annealing treatment increased the maximum discharge capacity of the multicomponent AB_2-type $Ti_{0.15}Zr_{0.85}La_{0.03}Ni_{1.2}Mn_{0.7}V_{0.12}Fe_{0.12}$ [19] and $Ti_{0.2}Zr_{0.8}La_xNi_{1.2}Mn_{0.7}V_{0.12}Fe_{0.12}$ ($x = 0.01–0.05$) alloys [20]. Additions of La (optimum content 3 wt% La) to both alloys improved their activation performance. Furthermore, higher discharge capacities were also achieved. However, the discharge capacity of the alloys decreases significantly when the current density increases. To achieve progress towards high power MH batteries development, it has been suggested that a nanocrystalline microstructure can improve the hydrogen storage performance by minimizing the amount of the secondary phases that do not contribute to the storage capacity and may allow to increase the diffusion rates of hydrogen in the alloys by having an increased amount of grain boundaries where the mobility of hydrogen is higher thus achieving advanced performance at high rates of charge and discharge of the Ni-MH batteries [21,22]. Furthermore, more homogeneous and refined phase distribution was achieved for the alloys by applying a Rapid Solidification process [23–25] which is also beneficial for their use as metal hydride anodes.

In the present study, Rapid Solidification technique was applied to the $Ti_{0.15}Zr_{0.85}La_{0.03}Ni_{1.2}Mn_{0.7}V_{0.12}Fe_{0.12}$ alloy to improve the rate performance of the anode electrode by producing nanostructured alloys [26,27]. The effect of variation of the wheel rotation speed on the crystal structure, morphology of the alloys' microstructures, phases abundance, electrochemical performance, and hydrogen diffusion properties of the non-stoichiometric C15 predominated alloys will be reported. In our earlier work [25], C14 predominated alloy with hexagonal structure prepared by rapid solidification was studied, and the obtained data will also be reviewed as a reference point in order to compare the electrochemical performances of the C15 and C14 types rapidly solidified alloys.

2. Experimental methods

The composition of the studied alloy was chosen as $Ti_{0.15}Zr_{0.85}La_{0.03}V_{0.12}Mn_{0.7}Fe_{0.12}Ni_{1.2}$ and contained a 10% excess of Mn as compared to the listed stoichiometry to compensate for a high rate of evaporation of Mn during the melting and casting. The alloy was prepared by arc melting of the alloying elements with a purity higher than 99.7% on a water-cooled copper hearth under argon atmosphere and re-melted three times to improve its homogeneity. The as-cast samples were then used for the rapid solidification casting performed in a SC Edmund Buehler melt spinner accommodated at Institut de Chimie de la Matière Condensée de Bordeaux (ICMCB, France) using the wheel rotation speeds of 5,

16.5, and 33 Hz. Parts of the as-cast alloy and the ribbon samples were crushed and mechanically ground, before separating a 40–60 μm fraction of the powder using a sieve. The fine powder with a size of less than 40 μm was used for the X-ray powder diffraction (XRD) measurements, which were performed by with a CuK_α radiation ($\lambda = 1.5418$ Å) by using a Rigaku MiniFlex 600 BenchTop X-Ray diffractometer having a flat plate geometry, with the measurements covering a range from 20° to 80° and with a step size of 0.01°. The experimental XRD data was processed by using Rietveld refinements and GSAS software [28].

The 40–60 μm powder which was used in the electrochemical measurements was mixed with a Carbonyl Nickel in a weight ratio of 1:4. This mixture was cold-pressed under a pressure of 12 MPa into a 10 mm pellet which was sandwiched between two nickel foams. The electrolyte used for the testing was a 9 M aqueous KOH solution. A half-cell was constructed using a MH alloy powder electrode as a working electrode, a platinum wire as a counter electrode and a mercury/mercury oxide (Hg/HgO) as a reference electrode. The metal hydride anode tests were performed at room temperature using a LAND CT2001A Battery Tester in an open-to-air flooded cell configuration against a partially pre-charged sintered $Ni(OH)_2$ counter electrode. 100 mA/g current density was applied to charge the electrodes for 5 h, then the same rate was applied to discharge the electrodes until a cut-off voltage of −0.7 V was reached.

For the microstructure characterization, bulk alloy and ribbon type samples were embedded in epoxy resin. The microstructures and the compositions of the samples were studied by LV-FE scanning electron microscopy (SEM) of the Zeiss Supra 55VP type.

To determine the hydrogen diffusion coefficient in the studied samples, Electrochemical Impedance Spectroscopy (EIS) characterization was performed [29] by using SP-300-Potentiostat from Bio-Logic Science Instruments. Galvanostatic Electrochemical Impedance Spectroscopy (GEIS) technique was applied in a range of frequencies from 1 kHz–0.5 mHz when using the current amplitude of 10 mA. Four different States of Charge (SoC) of the electrodes were selected for the studies, including SOC 0 (completely discharged anode), 30, 70, and 100 (fully charged anode) (%).

By assuming that the diffusion process is concentration independent, Fick's equation can be applied to calculate the hydrogen diffusion coefficient in the alloys which has an inverse square relation to the Warburg element [30]:

$$D_H = \frac{R^2T^2}{2A^2n^4F^4C^2\sigma^2}$$

where

D_H - diffusion coefficient of hydrogen
R - ideal gas constant
T - absolute temperature
A - electroactive surface area per unit volume of electrode
n - number of electrons transferred
C - concentration of hydrogen ions
σ - Warburg impedance coefficient.

The electrodes are considered as containing spherical particles which have a uniform size and are entirely exposed to the electrolyte. Thus, the electroactive surface area, A, can be determined using the equation [31]:

$$A = \frac{3(1-\in)}{r}$$

where

$\in$ = electrode porosity assumed to be 0.3 [32].
r = radius of spherical particles, an average value was 25 μm (see Experimental part).

3. Results and discussion

3.1. XRD analysis

The XRD patterns of four studied materials (as cast and melt-spun samples at 5, 16.5 and 33 Hz samples) are shown in Fig. 1 (a). Both as-cast and melt-spun samples consist of a cubic C15 type Laves phase as the main constituent and C14 phase as a minor phase. Rietveld refinements showed that the abundance of the C15 phase is higher than 70 wt% for every studied material.

Clearly distinguishable peaks (103) and (112) of the hexagonal C14 phase disappeared after applying the rapid solidification at a rate of 5 Hz indicating that the abundance of the C14 phase significantly decreased.

A typical plot of Rietveld refinements performed using GSAS software for the sample solidified at 16.5 Hz is shown in Fig. 1 (b). The refinements yielded the abundances of C15 and C14 phases, unit cell volumes of the C15 and C14 phases, and the crystallite sizes of C15 phase which are given in Table 1. We note that the crystallite size for the minority C14 phase was not determined because of its low abundance.

From the presented in Table 1 data, we conclude that:

(a) The crystallographic data of as-cast and melt-spun samples well agree with the results of our earlier publication [19]. Addition of 10 wt% Mn to the alloy causes an increase of the unit cell volume for the C15 phase [33]. This is as expected, as Mn has a larger atomic radius (1.264 Å) than Ni (1.246 Å); thus, a partial replacement of Ni will cause enlargement of the lattice parameter of the alloy. We furthermore note that the alloy with the higher content of Ti studied in Ref. [20] shows the smallest unit cell volume of the C15 intermetallic as compared to the results of the present study. The cell parameters of the C15 Laves phases decrease as the amount of Ti increases due to the fact that a smaller in size Ti atom (1.462 Å) substitutes for a larger Zr atom (1.602 Å) in the crystal structures of the alloys [34]. In addition, we also observe that C14 phase identified as the main component of the $Ti_{12}Zr_{21.5}V_{10}Cr_{7.5}Mn_{8.1}Co_8Ni_{32.2}Al_{0.4}Sn_{0.3}$ alloy studied in our earlier work also showed a smaller unit cell volume as compared to the current study showing the effect of increased Mn content in the present work.
(b) The crystallite size of the C15 phase (around 80 nm in average) remained unchanged during the rapid solidification process.
(c) When rapid solidification was applied at 5 Hz rotation speed, the abundance of the C15 phase became higher. As the rotation speed increases further to 16.5 and 33 Hz, the abundance of C15 phase becomes lower than at 5 Hz speed indicating that the C15 phase is more likely to form at lower solidification rates as compared to the C14 phase. This phenomenon was also observed in an earlier report [35].
(d) At 16.5 Hz rotation speed, the melt-spun sample shows the largest unit cell volume for both C15 and C14 phases, while for the 33 Hz melt-spun alloy an opposite trend is observed.

In contrast, the rapid solidification process performed on C14 predominated alloy [25] produced a different outcome. As the wheel rotation speed increased, the abundance of the C14 phase became higher, indicating that the C14 phase is preferably formed

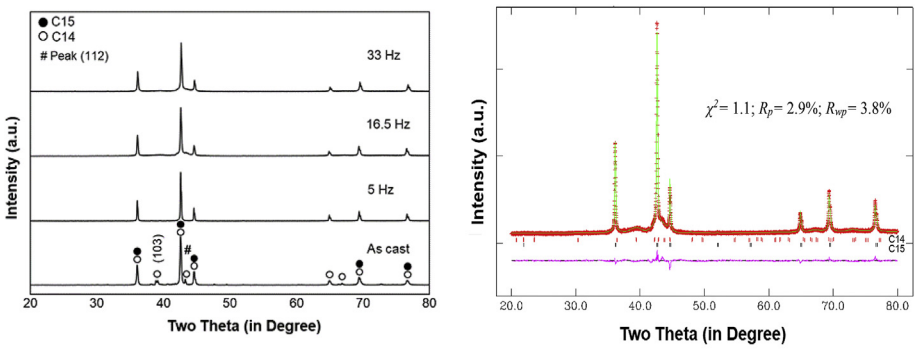

Fig. 1. XRD patterns (Cu-K_α) for as-cast and melt-spun samples of the alloy $Ti_{0.15}Zr_{0.85}La_{0.03}Ni_{1.2}Mn_{0.70}V_{0.12}Fe_{0.12}$ prepared at different wheel rotation speeds of 5, 16.5, and 33 Hz. Two Laves phases (C15 and C14) can be identified (a). Observed (+), calculated (upper line), and difference (lower line) Rietveld GSAS refinement plots of the XRD pattern of the 16.5 Hz melt-spun sample are shown as an example. The refined abundances of the intermetallics are: C15 (80 wt%) and C14 (20 wt %) (b).

Table 1
Phase abundances and crystallographic data for the C15 and C14 Laves type intermetallics.

Alloy	C15					C14				
	a, Å	V, Å^3	Crystallite size, nm	Abundance, wt.%	Reference data a (Å), V (Å^3)	a, Å	c, Å	V, Å^3	Abundance, wt.%	Reference data a, c (Å), V (Å^3)
As cast	7.0236(1)	346.5(2)	42	76.7(4)	7.0235(1) 346.47(1) [19]	4.9848(3)	8.1516(9)	175.4(2)	23.3(2)	4.9662(1)
5 Hz	7.0289(4)	347.3(7)	49	100		–				8.0935(2)
16.5 Hz	7.0391(8)	348.8(1)	41	80.0(3)	7.0163(1)	4.9645(1)	8.1600(5)	174.2(2)	20.0(2)	172.9(1) [25]
33 Hz	7.0156(8)	345.3(1)	42	78.7(3)	345.40(1) [20]	4.9481(1)	8.1486(3)	172.8(1)	21.3(3)	

at higher solidification rates compared to the C15 phase. The crystallite size for the C14 phase significantly decreased from the initial 104 nm for the as-cast alloy to 21 nm for the melt-spun sample at 100 Hz. The smallest crystallite size sample produced at the highest rotation wheel speed resulted in the best electrochemical performance by allowing the shortest H atoms diffusion distances.

3.2. SEM/ EDS analysis

Microstructures of as-cast and melt-spun samples were studied using SEM in a back-scattered electron (BSE) mode and are presented in Fig. 2.

Changing the wheel rotation speed which proportionally changed the solidification rate, modified the phase-structural composition, morphology and microstructure of the alloys. The alloys contained 3 different phases including C15, C14, and La-rich phase. The grain size of each phase depends on a wheel rotation speed. With an increase in the wheel rotation speed, the grain size decreases. The as-cast sample contained a three-phase microstructure with the main C15 Laves type intermetallic having a grain size of approximately 3.5 μm. The grain size was slightly lower, 2 μm, for the secondary C14 intermetallic phase, while for the La-rich phase it got a size of 2.9 μm (see Fig. 2).

Applying rapid solidification yielded the following results:

(a) Refinement of the microstructures took place. When the higher rotation speeds are applied, a decrease in the grain size was observed. At a 5 Hz rotation speed the grain size of C15 phase dramatically drops from the initial 3.5 μm to just approximately 500 nm and further down to 300 nm at 33 Hz.
(b) An increase in the rotation speed causes formation of more homogeneous and refined microstructures. La-rich phase seen as white globular particles became smaller and more evenly distributed in the 5 Hz melt-spun sample as compared to the as-cast sample, with the grain size of approximately 375 nm. Formation of La-rich globular particles have also been reported for the similar alloy compositions in reference publications [36,37]. C14 intermetallic phase has a decreased grain size of 200 nm.
(c) At 16.5 Hz, smaller grain sizes of C15 phase, 300 nm, and C14 phase, 175 nm, were formed, and La-rich white globular structures with just 250 nm in grain size became more evenly and regularly distributed as compared to the 5 Hz melt-spun sample.
(d) The smallest grain size for the main C15 phase of 250 nm, 100 nm for the secondary C14 phase, and 70 nm of the La-rich phase appeared when applying 33 Hz rotation speed. The dendritic structures were formed by applying this casting speed. C15 phase forms more homogeneous structures [38] which create less nuclei sites required for the solidification. Because of that, a homogeneous nucleation is taking place. When the solidification rate increases, a supercooled liquid of C15 phase forms which then solidifies and produces dendritic microstructures [39].

Similar phenomena were also observed in rapidly solidified C14-predominated alloys [25]. Here also more uniform and refined microstructures were produced during the rapid solidification process. However, significant morphology variations of the melt-spun samples were found in C14 predominated alloys. Increased rate of rapid solidification caused formation of a dendritic microstructures at 16.5 Hz and at 33 Hz. In contrast, at the highest rotation speed of 100 Hz, the morphology becomes more uniform with a matrix C14 phase composing a core and a secondary C15 phase forming a shell. Furthermore, the dendrite structure was no longer observed.

This paper contains the Supplementary Materials data which includes 3 Figures (Figs. S1, S2, and S3) and 3 Tables (Tables S1, S2, and S3). The EDS/ SEM micrographs for as-cast, and rapidly

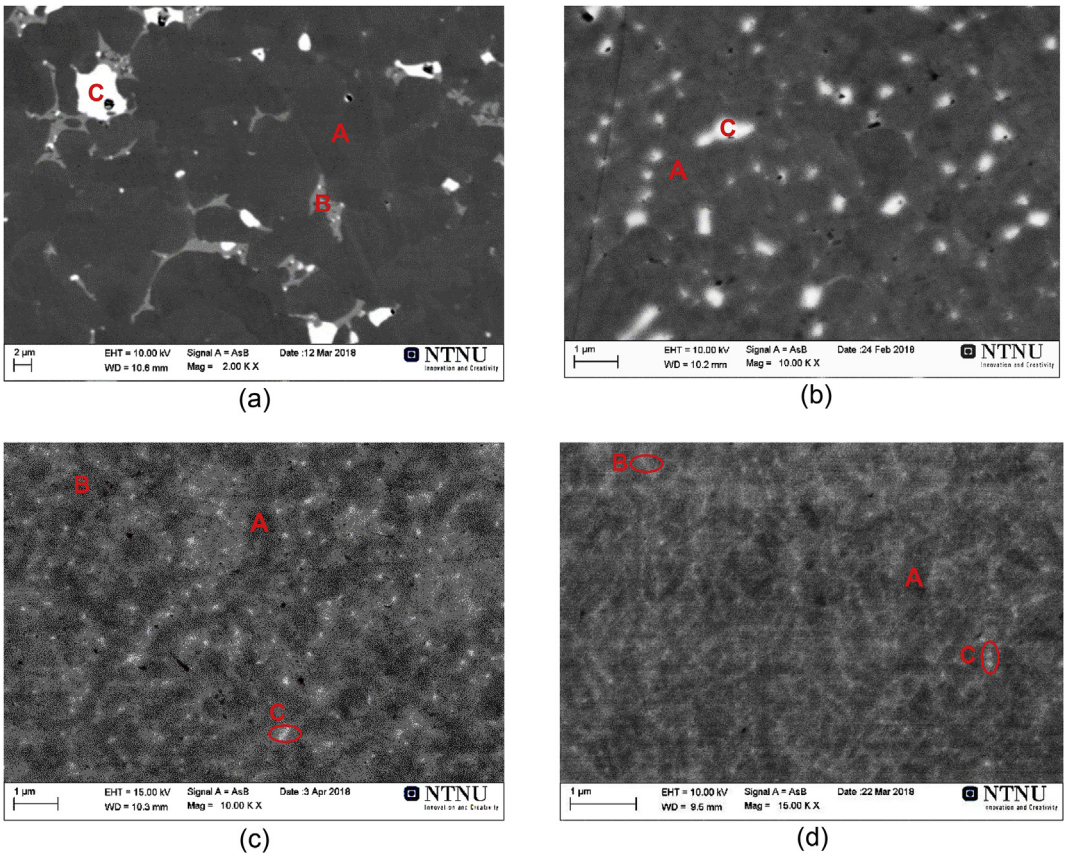

Fig. 2. SEM BSE images of as-cast (a) and melt-spun samples obtained at variable rotation speeds of 5 Hz (b), 16.5 Hz (c), 33 Hz (d). The sample contains 3 different phases, A: matrix phase (C15), B: secondary phase (C14), and C: La-rich phase. Decreasing grain size of matrix phase from 3.5 µm for the as-cast down to 250 nm achieved during the Rapid Solidification can be noticed.

solidified at 5, and 16.5 Hz samples are shown in Fig. S1, while the EDS analysis results for as-cast, 5, and 16.5 Hz melt-spun samples are given in Table S1. The darker area of EDS images (see Fig. S1) represents the matrix phase, while the lighter area (grey) shows the secondary phase, and the white globular area located on the secondary phase is La-rich phase.

33 Hz melt-spun sample has been characterized by Auger electron spectroscopy (AES) to determine the surface compositions by analyzing the electronic state energies of the constituent elements (see Fig. 3). The data showing the mapping of the elemental distribution is shown in Fig. 3. We conclude that La-rich phase formed as a secondary phase which dissolved another A-element, Zr, but also it contained less Ni as compared to the reference LaNi secondary intermetallic [19,20]. These changes affected the hydrogenation performance of the La-rich phase.

From the data presented in Tables S1 and S2 we can draw the following conclusions.

(a) The data of EDS and Auger spectroscopy measurements shows a very uniform homogeneous distribution of constituent elements in the studied samples. Indeed, only slight variations of elementary content were observed during the parallel measurements (see Table S1 and Table S2). Matrix phase contains Zr and Ti as A components, with almost no La present. The B component mixture is dominated by Ni and Mn, with a significantly smaller contributions from V and Fe (see Fig. S2). The matrix phase also contained oxygen, but its amount is reasonably modest. The compositional change for the matrix phase takes place during the Rapid Solidification, particularly for the Mn and Ni amount. A gradual decrease in the content of Mn is taking place from as-cast to 33 Hz sample (by appr. 32%) indicating that Mn is subjected to a profound evaporation during the rapid solidification process. Furthermore, the amount of Ni increases from as-cast to 33 Hz sample suggesting that enrichment by Ni takes place for the matrix phase because of a decay in Mn content.

(b) The La-rich secondary phase studied in Refs. [19,20] and acting as a catalyzer of the hydrogenation of the matrix phase was La-rich and contained a LaNi intermetallic. It appears that rapid solidification caused the change in the composition of this phase, and further to La and Ni, it also included Zr and Mn. This brings us to a conclusion that rapid solidification causes a significant solubility of Zr in the LaNi-based secondary phase which also dissolves Mn.

Furthermore, the secondary phase contains a significant amount of oxygen as its level is 3 times higher than O content in the matrix Laves phase. Because of a significant amount of zirconium and oxygen present, the secondary phase becomes unable to act as a catalyst of hydrogenation causing a very slow and difficult activation of the alloys. Probably the conditions of rapid solidifications need to be changed to benefit from an easy activation behavior of the LaNi intermetallic as observed in Refs. [19,20].

There are two reasons for the observed difficulties in the hydrogenation and in electrochemical charging performance of the anode electrode alloy.

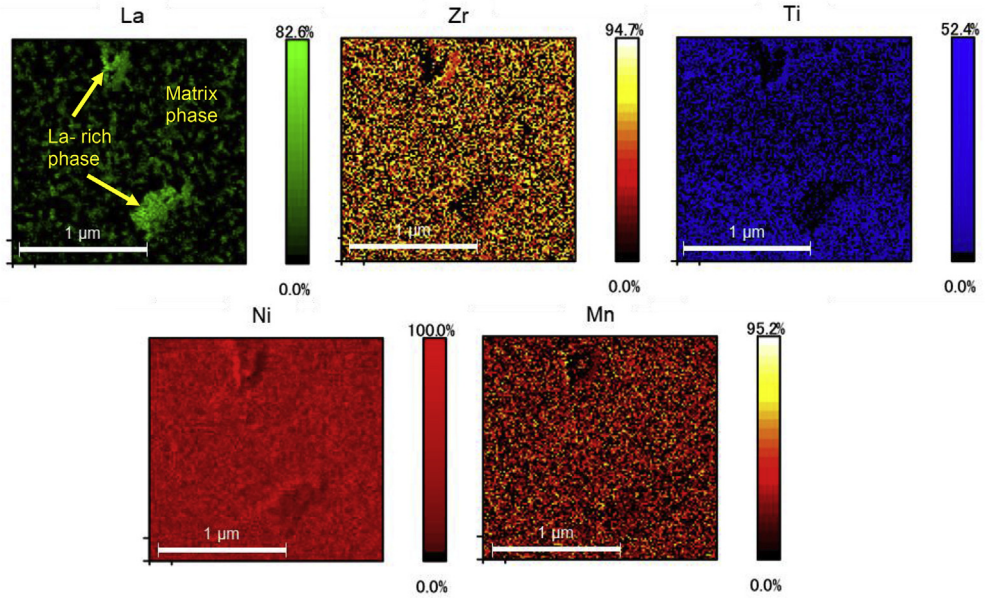

Fig. 3. The elemental mapping obtained by using the data of Auger analysis of the 33 Hz melt-spun sample shows presence of two phases – a matrix phase and a secondary La-rich phase, even though the XRD analysis of the sample confirmed presence of two Laves phases, C15 intermetallic (78.7%) and C14 phase (21.3%). However, because of a very similar chemical composition, these phases are indistinguishable in the Auger spectroscopy data. We also note a homogeneous distribution of Zr, Ti, Ni and Mn in the matric phase.

(a) During the solidification of the initial as cast alloy, LaNi intermetallic compound is formed which is known to actively form the hydride phase $LaNiH_{3.6}$. The annealing does not change the fact that the microstructure of the alloy shows presence of the Laves type intermetallic together with a secondary LaNi-based phase compound. However, during the rapid solidification the composition of the LaNi alloy becomes modified by a partial replacement of La by a smaller in size Zr. (La,Zr)Ni intermetallic has a lower affinity to hydrogen and is not able to quickly and actively form a hydride phase. Thus, a catalytic influence of (La,Zr)Ni intermetallic does not appear to be present anymore and thus activation performance worsens.

(b) Furthermore, as zirconium has a strong affinity to oxygen, as it easily oxidizes. Such oxidation is mostly limited to the surface layers because of the presence of trace amounts of oxygen in argon gas during the rapid solidification. The formation of the surface oxides creates a barrier for hydrogen atoms for their diffusion into the bulk and thus decreases the catalytic activity of the alloy to absorb hydrogen and to form a metal hydride.

Further to the elemental mapping using Auger analysis, by analyzing the areas occupied by the secondary phase (see Fig. 3 and Table S3), we conclude that the secondary phase is enriched with La and contains significant amounts of Zr. This is opposite to the situation in the as cast alloy where LaNi intermetallic is formed instead, with no Zr solubility observed.

3.3. Electrochemical measurements

The activation performances of as-cast and melt-spun alloys are presented in Fig. 4 (a). Metal hydride anodes were charged at a current density of 100 mA/g for 5 h followed by a 30 min rest and then discharged at a current density of 100 mA/g to a voltage cut–off of −0.7 V against the Hg/HgO reference electrode. After the anodes were fully activated, they were charged at a current density of 100 mA/g followed by a 30 min rest and discharged at different current densities (10–500 mA/g) to a voltage cut-off of −0.6 V against the Hg/HgO reference electrode.

It appeared that the melt-spun samples required a longer cycling to reach a complete activation as compared to the as-cast alloy. It is likely that rapid solidification process increased the content of oxides in the surface layer of the melt-spun samples and because of that they required a higher number of the charge-discharge cycles to remove the oxide barriers and to allow a fast charge-discharge process. In addition, a more increased Zr content in the secondary phase due to the rapid solidification process causes a worse activation performance. The secondary phase does not act any more as a catalyst capable of accelerating the hydrogenation of the matrix phase.

For the as-cast alloy its maximum capacity was achieved already in the fourth cycle, while for the 5 Hz sample 7 cycles were needed to activate it, and 33 Hz sample needed 6 cycles to get fully activated. The most difficult activation performance was observed for the 16.5 Hz sample. Even 11 cycles were not sufficient to activate the sample. However, the full activation capacity of this sample results in the same capacity as for the 5 Hz alloy, 306 mAh/g. We note that the activation capacity of the 5 Hz samples is 50% higher than for the 33 Hz, 306 mAh/g and 181 mAh/g, respectively. Higher activation capacity achieved for the 5 Hz sample could be due to the optimized microstructure of the sample that shows a significant refinement as compared to the other samples. To conclude, rapid solidification process improved the maximum discharge capacity of as-cast alloy which was limited to 273 mAh/g only (this is smaller than in our earlier publication due to the excess of Mn added to the presently studied alloy [19]), while a greater number of cycles was required to activate the alloys.

Fig. 7 (b) shows discharge capacity vs. discharge potentials for as-cast and melt-spun alloys measured at 100 mA/g current density. It can be noted that together with a larger discharge capacity, 5 and 16.5 Hz, melt-spun alloys also show longer and flatter plateau of discharge potentials which are located between −0.85 and −0.9 V indicating that these samples achieve more stable and better performance as compared to the other samples.

In the case of rapidly solidified C14 predominated alloys [16],

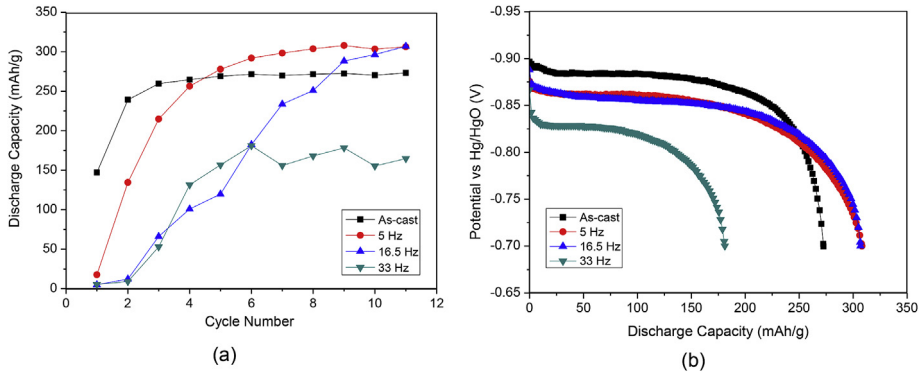

Fig. 4. Activation performance (a), discharge capacity vs potential (b), of the as-cast and melt-spun alloys at 100 mA/g discharge current density.

melt-spun alloys also showed a poorer activation performance as compared to the as-cast alloy. Indeed, more than 15 cycles were not enough to activate the as-cast alloy giving an indication that C14 predominated alloy is more difficult to activate than C15 alloy. Inferior activation performance of the samples obtained by rapid solidification process is likely to be caused by the presence of a thicker oxide layer on their surface.

Furthermore, by varying the wheel rotation speed, morphology of the microstructures significantly changes, thus affecting the electrochemical properties of the melt-spun samples. The best rate performance is achieved for a 16.5 Hz melt-spun sample which reached 414 mAh/g discharge capacity at 10 mA/g current density, followed by 5 Hz, as-cast, and 33 Hz samples (see Fig. 5 (b)). The discharge capacities vs. discharge potentials for 16.5 Hz sample measured at different current densities are shown in Fig. 5 (a). We note that an excellent rate performance was achieved for this sample at high current densities. Thus, the formation of the optimized refined microstructure results in the best rate performance.

For the HRD performance (the ratio between the capacities obtained at the highest current density of 450 mA/g to the lowest current density of 10 mA/g), 16.5 Hz sample shows the best HRD performance by showing the smallest decrease in the capacity at increasing current densities (see Fig. 5 (c)). At the same time, 33 Hz sample shows a rapid decrease in the capacity at a current density

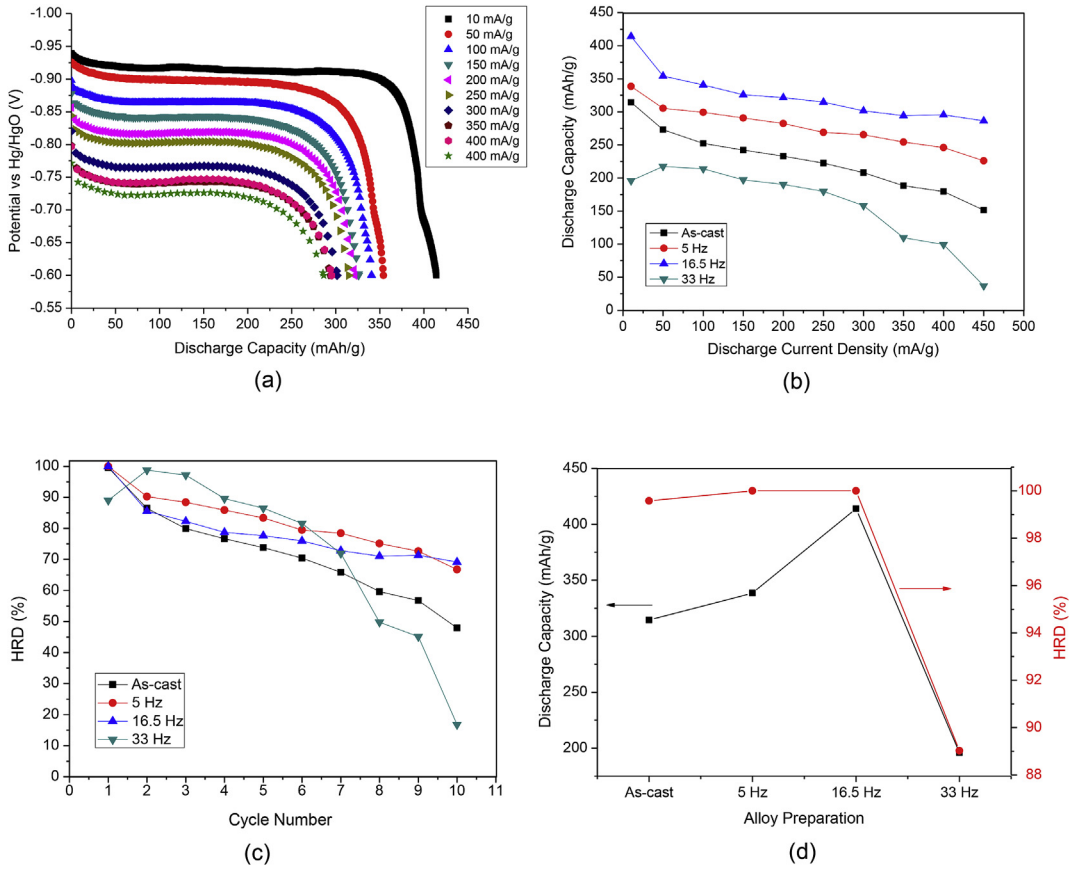

Fig. 5. The capacity of the melt-spun 16.5 Hz alloy electrode at variable discharge current densities and cut-off potentials (a); rate performance of the as-cast and melt-spun alloys (b); HRD performance (c); comparison of the performance of the samples as related to the conditions of alloys preparation (d).

exceeding 100 mA/g. After reaching a current density of 100 mA/g, capacity markedly dropped. The dendritic microstructure is considered as a reason for this decline in the performance.

Rapid solidification significantly changes the phase-structural composition of the alloys and because of that it affects the activation behavior and HRD performance. The C15 Laves phase predominant samples show a more developed pulverization and form more homogeneous microstructures with less C14 phase present in the melt-spun alloy which correlates with their better activation performance. On the other hand, the optimized microstructure which is formed by reaching an appropriate ratio between C15 and C14 phases benefits from a synergetic effect of C15 intermetallic with high hydrogen diffusivity and C14 intermetallic with H storage capacity resulting in improved rate performance of the metal hydride anode electrodes. Importantly, rapid solidification process proved to significantly refine the microstructure thus reducing the distances of hydrogen atoms diffusion and creating a faster hydrogen diffusion paths through the structure (see Fig. 5 (d)). We note that the improvement of the rate performance of the melt-spun alloys was achieved at 16.5 Hz melt-spun sample.

In the case of rapidly solidified C14-predominant alloy, it was observed that the rapid solidification improves the HRD performance of the melt-spun sample at the highest wheel rotation speed [16]. Thus, producing a homogeneous refined microstructure of the metal hydride anode materials with an optimized ratio C14/C15 which was achieved for the highest applied solidification rate will result in the best electrochemical performance. This is associated with the smallest crystallite sizes observed for such an alloy resulting in the fastest hydrogen diffusion in the material.

These studies showed that phase-structural composition and electrochemical performance of these alloys can be modified by selecting and optimizing conditions of rapid solidification, allowing to tailor their properties. As examples, (a) for A_2B_7 alloys melt spinning resulted in an increased abundance of the AB_5 phase acting as a catalyst activating the $(La, Mg)_2Ni_7$ phase [40]; (b) for La_2MgNi_9 alloy, appropriate conditions of its rapid solidification and adjustment of Mg content in the initial material resulted in increased content of La_2MgNi_9 with increase of the electrochemical capacity [41]; (c) Optimization of the rate of the wheel rotation speed allowed to reach maximum discharge capacity of 323 mAh/g for the $Mm(NiCoMnAlV)_5$ alloy [42]. However, in case of the AB_2 alloy, even though a maximum discharge capacity of 385 mAh/g was achieved for the melt-spun $Zr_{0.7}Ti_{0.3}Mn_{0.4}V_{0.4}Ni_{1.2}$ alloy electrode, however a large number - approximately 25 cycles - were needed to reach the maximum activation capacity [43]. Thus, activation of the melt-spun processed $Zr_{0.7}Ti_{0.3}Mn_{0.4}V_{0.4}Ni_{1.2}$ alloy required improvements – similar to the results of the present study for the $Ti_{0.15}Zr_{0.85}La_{0.03}V_{0.12}Mn_{0.7}Fe_{0.12}Ni_{1.2}$ alloy after the rapid solidification.

The $Ti_{0.15}Zr_{0.85}La_{0.03}V_{0.12}Mn_{0.7}Fe_{0.12}Ni_{1.2}$ alloy prepared in the current study using melt-spinning at 16.5 Hz wheel rotation speed showed a superior compared to the reference data discharge capacity of 414 mAh/g. The tailoring of the chemical composition achieved due to the rapid solidification led to the improved electrochemical performance of the electrode. However, increased amount of oxygen present in the alloy after the rapid solidification and introduction of Zr into the composition of La-rich phase caused difficulties in its activation. Therefore, controlling the content of oxygen and conditions of rapid solidification are the most important factors to achieve the improved electrode performance. Controlled addition La to the alloy is one of the alternatives to reduce the amount of oxygen as lanthanum is capable in refining the alloys from O thus making the surface of the alloy cleaner because of the reduced content of oxide at the surface. Furthermore, optimum conditions of rapid solidification need to be selected to achieve improved electrochemical behaviours of the metal hydride anode electrodes.

3.4. Electrochemical Impedance Spectroscopy (EIS) characterization

To determine the hydrogen diffusion coefficient in the studied materials, EIS studied were performed for the selected samples, including as-cast alloy, 16.5 Hz, and 33 Hz materials. The EIS data show a clear interrelation between the conditions of the rapid solidification and the hydrogen diffusion characteristics.

Two series of equivalent circuits were used to fit the Nyquist impedance plots (see Fig. 6). Constant Phase Elements (CPE) were used as pseudo-capacitance to describe the depressed semicircle shape of Nyquist impedance plot indicating the surface inhomogeneity/ surface roughness or other effects that possibly cause uneven current distributions at the electrode surface [23]. By using pseudo-capacitance CPE in the equivalent circuit, a much better fit of the EIS was achieved. Furthermore, in the present study, two parallel circuits were connected in series to achieve a more accurate modelling of the studied electrode. These models were successfully utilized to fit the experimental Nyquist impedance plots.

The equivalent circuit elements shown in Fig. 6 include R_{el} (electrolyte resistance), $R_{contact}$ (contact resistance between alloy particles and current collector), $R_{charge\ transfer}$ (charge transfer resistance on the interface between electrode and electrolyte), and Warburg element (capacitance of the electrode surface exhibiting the mass transport limitation related to hydrogen diffusion).

Nyquist impedance plots, the experimental and fitted ones, for the selected samples including as-cast, 16.5 Hz, and 33 Hz are shown in Fig. 7. It could be noted that the melt-spun alloys show significantly different EIS plots as compared to the as-cast sample. The data for the as-cast sample contains only one large semicircle, with a very small Warburg element in its low frequency region for all SOC, while EIS data for the 16.5 and 33 Hz samples show presence of two semicircles and a developed Warburg element at all SOC. To account for the insufficiently developed Warburg component for the as-cast sample, a parallel Randles circuit was used to fit the Nyquist impedance plot. For both melt-spun samples it was necessary to use 2 equivalent circuits connected in series and this allowed to achieve an appropriate fitting (Fig. 7).

The numerical fitting results of two main semicircles parts with one tail of Warburg element show quite a significant difference in properties. After applying the rapid solidification to the alloy, Warburg element becomes more pronounced while the Nyquist impedance plot becomes split showing a different shape, which indicates the changes of contact and charge transfer resistances. Furthermore, almost all the fitting parameters including CPE charge transfer, contact resistance of the alloy particle and current collector, and Warburg element decreased, indicating that the rapid solidification reduced the total resistance of the alloy electrodes (see Fig. 7 b and c). 16.5 Hz sample shows the smallest total resistance, while 33 Hz sample shows an opposite behavior. Thus, 16.5 Hz appears to be the optimized wheel rotation speed which

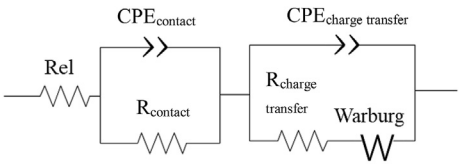

Fig. 6. Modified equivalent circuit which contains two parallel circuits, R-CPE and Randles circuits, to fit the Nyquist impedance plot.

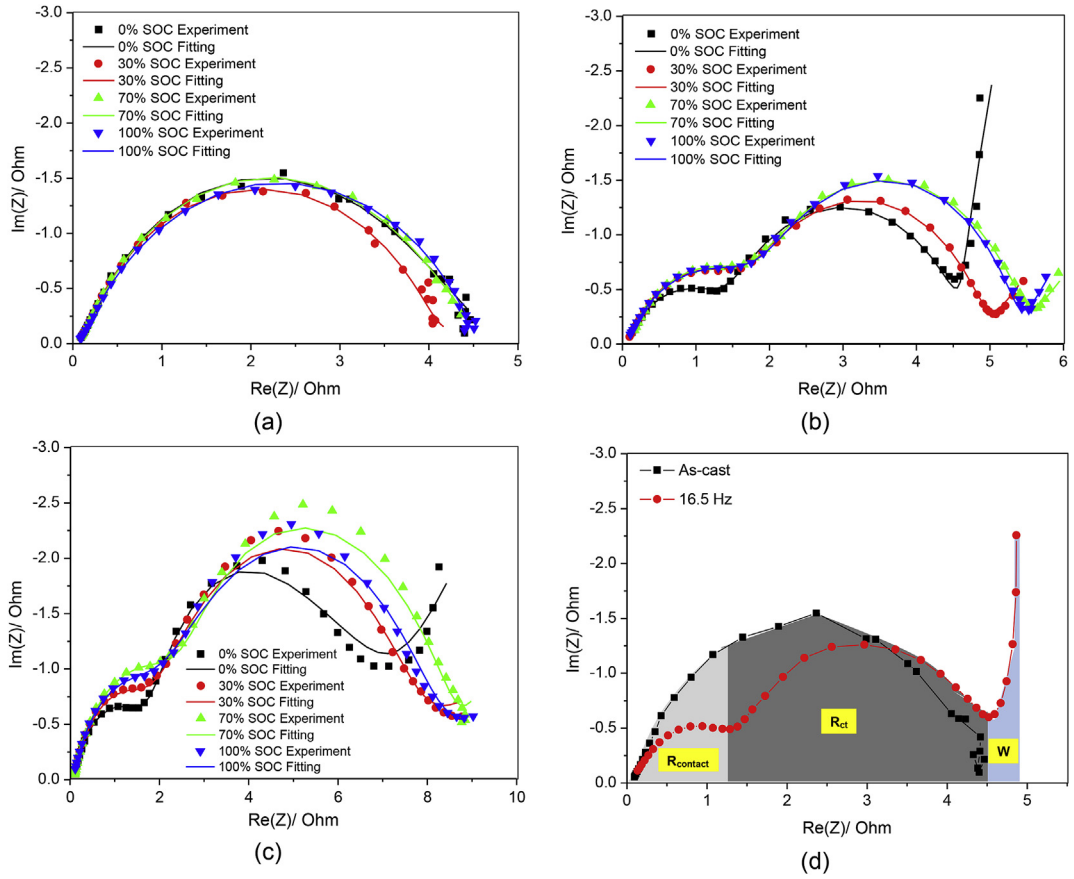

Fig. 7. Nyquist impedance plots, including the experimental and the fitted data for the 0, 30, 70, and 100% SOC electrodes measured for the as-cast (a), 16.5 Hz (b), and 33 Hz (c) alloys. Two modified equivalent circuits (see Fig. 6) were used to fit the EIS spectra. Split of one semicircle for as-cast sample into two semicircles for the melt-spun samples indicates a significant change in their electrochemical behavior (d). Rapid solidification enhances the contact resistance (R_{ct}) and Warburg element (W) of the samples.

produces the best discharge capacity by achieving the smallest total resistance and by having the highest hydrogen diffusion coefficient (see Table 2). The grain refinement which was caused by applying rapid solidification decreased the contact resistance between the refined alloy particles and the current collector. Indeed, the decreasing CPE for charge transfer in the melt-spun samples can originate from the improvement of the surface homogeneity of the alloy and the enlargement of the surface-active area of the alloy. However, charge transfer resistance of the as-cast is smaller than the values for the melt-spun samples. Interestingly, increasing of Rct for all SOC in the melt-spun samples gives a less pronounced effect on the hydrogen diffusion as compared to the decreased value of the Warburg element.

The diffusion coefficient of hydrogen appears to be significantly

Table 2
Fitted parameters of EIS spectra for the as-cast and melt-spun samples.

Parameters	0% SOC			30% SOC			70% SOC			100% SOC		
	As-cast	16.5 Hz	33 Hz	As-cast	16.5 Hz	33 Hz	As-cast	16.5 Hz	33 Hz	As-cast	16.5 Hz	33 Hz
$R_{electrolyte}$, Ohm	0.02504	0.09234	0.1164	0.01644	0.08047	0.09197	0.01678	0.08823	0.09024	0.0116	0.07254	0.09727
$CPE_{contact}$, $F.s^{\alpha-1}$	0.02303	0.03028	0.02002	0.02866	0.02766	0.02105	0.02769	0.02539	0.02276	0.03533	0.02893	0.02243
n_1	0.8618	0.7313	0.8139	0.808	0.7154	0.7762	0.7879	0.7407	0.7607	0.7491	0.706	0.7733
$R_{contact}$, Ohm	3.008	1.391	1.442	3.52	1.799	1.805	4.043	1.745	2.297	4.252	1.858	1.951
CPE_{ct}, $F.s^{\alpha-1}$	0.5512	0.4212	0.3034	1.622	0.2772	0.2235	2.749	0.2645	0.2193	3.893	0.3098	0.2144
n_2	0.1891	0.8854	0.7779	0.1186	0.8646	0.794	0.06414	0.8555	0.8133	0.046	0.872	0.773
R_{ct}, Ohm	0.05817	2.771	5.167	0.06902	3.01	5.558	0.08032	3.361	5.864	0.09654	3.019	5.924
σ, $Ohm.s.^{1/2}$	3.628	0.07426	0.1017	3.379	0.02881	0.0982	3.192	0.02659	0.0908	2.869	0.02501	0.05906
Goodness of fit, χ^{2*}	0.2236	0.07066	0.4276	0.05787	0.02054	0.2197	0.01655	0.02072	0.5088	0.01626	0.02741	0.2029
D_H, $cm^2.s^{-1}$	8.21E-14	1.96E-10	1.05E-10	9.47E-14	1.30E-09	1.12E-10	1.06E-13	1.53E-09	1.31E-10	1.31E-13	1.73E-09	3.10E-10

$^*\chi^2 = \sum_{i=1}^{n} \frac{\left|Z_{means(i)} - Z_{model}(f_i, param)\right|^2}{SD_i^2}$.

where

Z_{meas} (i) = measured impedance at f_i frequency

Z_{model} (f_i, param) = function of chosen model

f_i = frequency

param = model parameters: $R_{electrolyte}$, $R_{contact}$, $CPE_{contact}$, CPE_{ct}

SD_i = standard deviation

affected by Warburg element as an inverse square of Warburg element is proportional to the H diffusion coefficient, according to a simplified equation of Fick's diffusion (see the experimental part). It appears that for the studied materials Warburg element becomes the most pronounced in the case of 0% SOC. The decrease of Warburg element indicates an increase in hydrogen diffusion coefficient, with 16.5 Hz having the larger reduction of Warburg element as compared to the 33 Hz alloy. Thus, 16.5 Hz alloy has the largest hydrogen diffusion coefficient among the studied materials.

In our earlier publication [25] we observed that the best electrochemical discharge for the alloy with the smallest size of the crystallites which was obtained at the highest wheel rotation speed. Similarly, the 16.5 Hz melt-spun sample showed the presence of the smallest crystallites and a larger unit cell volume among other studied materials thus allowing the fastest diffusion of H atoms with the largest hydrogen diffusion coefficient and the shortest H diffusion distances. The smallest crystallite size allowed to get the lowest contact resistance which was beneficial when SoC of the samples increased. Further to this, the optimized ratio between C15 and C14 phases contributed to assist the faster hydrogen diffusion in the multiphase alloy.

For all studied materials at 0% SOC the hydrogen diffusion coefficient appears to be significantly lower. By increasing SOC during a transformation from α-solid solution to the hydride phase, the hydrogen diffusion dramatically increases following an extent a transformation into the hydride ranging from 30 to 100% SOC (Fig. 8). Transforming the α-solid solution into the hydride phase changes intrinsic properties of the hydrogen-containing materials, with higher diffusion rates observed for the hydride thus leading to the increase of D.

4. Conclusions

- Rapid solidification of a Laves type C15 predominated $Ti_{0.15}Zr_{0.85}La_{0.03}V_{0.12}Mn_{0.7}Fe_{0.12}Ni_{1.2}$ alloy has been performed at 5, 16.5, and 33 Hz of wheel rotation speeds and resulted in changes which strongly affected alloys performance as anode materials of the Ni-MH battery, including
  (a) changes in a ratio between the main C15 and the secondary C14 phases;
  (b) a gradual decrease in the grain size from the initial 3.5 μm size down to 250 nm;
  (c) modification of the morphology of the microstructures;
  (d) changes in the discharge capacity, activation properties, and high rate discharge performance as related to the metallurgical and phase-structural state of the alloys.
- The melt-spun alloys show a more difficult activation performance as compared to the as-cast sample. These changes are associated with introduction of Zr into the composition of the secondary La-and Ni-rich phase during the melt casting at high speeds and rapid cooling/quenching of the alloy. Presence of Zr causes a worsening of the hydrogenation rates as compared to LaNi itself as in Refs. [19,20]. In present study, rapid solidification resulted in the formation of (La,Zr) (Ni,Mn) secondary phase appearing in the melt-spun samples while the La-rich intermetallic also contained a significant amount of oxygen. Thus, La-rich secondary phase was not acting as a catalyzer of hydrogenation anymore and because of that the activation performance significantly worsened. Optimization of the rapid solidification conditions is required to achieve a quick activation behavior of the Laves type metal hydride anode alloys.
- 16.5 Hz alloy provided the best rate performance because of an optimum two-phase microstructure containing C15 and C14 phases.
- Diffusion coefficient of hydrogen shows a close interrelation with SOC of the electrode and increases for all materials reaching the highest value for the completely charged electrodes with the smallest values observed for the completely discharged anodes.
- As the present alloy satisfies the high entropy alloys definition, the HEA concept may contribute to the design of new functional materials for battery anodes.

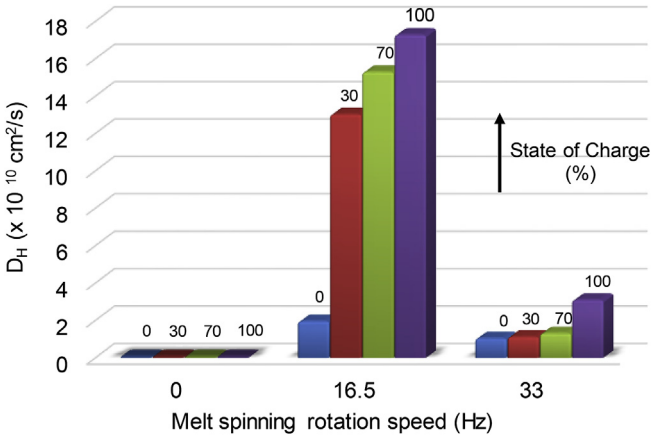

Fig. 8. Hydrogen diffusion coefficient (D_H) for as-cast and melt-spun alloys as related to SOC of the electrodes. The blue bars in the Figure show much smaller values of hydrogen diffusion coefficient observed at 0% SOC as compared to the coefficients at higher values of SOC with the highest values of D_H observed for the completely charged electrodes. (For interpretation of the references to colour in this figure legend, the reader is referred to the Web version of this article.)

Acknowledgements

This work was supported by Indonesia Endowment fund for Education (LPDP) and a PhD research project at Norwegian Research Center on Zero Emission Energy Systems for Transport (MoZEES). We thank CNRS Bordeaux and NTNU for the availability of the laboratory facilities for the rapid solidification process, and BASF-Ovonic Rochester Hills, USA for the access to their research laboratories.

Appendix A. Supplementary data

Supplementary data to this article can be found online at https://doi.org/10.1016/j.jallcom.2019.06.324.

References

[1] G.G. Libowitz, H.F. Hayes, T.R.P. Gibb, The system zirconium–nickel and hydrogen, J. Phys. Chem. 62 (1958) 76–79.
[2] T. Sakai, K. Oguro, H. Miyamura, N. Kuriyama, A. Kato, H. Ishikawa, C. Iwakura, Some factors affecting the cycle lives of $LaNi_5$-based alloy electrodes of hydrogen batteries, J. Less Common Met. 161 (1990) 193–202.
[3] J. Willems, K. Buschow, From permanent magnets to rechargeable hydride electrodes, J. Less Common Met. 129 (1987) 13–30.
[4] F. Feng, M. Geng, D.O. Northwood, Electrochemical behaviour of intermetallic-based metal hydrides used in Ni/metal hydride (MH) batteries: a review, Int. J. Hydrogen Energy 26 (2001) 725–734.
[5] B. Paxton, J. Newman, Modeling of nickel/metal hydride batteries, J. Electrochem. Soc. 144 (1997) 3818–3831.
[6] V. Yartys, D. Noreus, M. Latroche, Metal hydrides as negative electrode materials for Ni–MH batteries, Appl. Phys. A 122 (2016) 43.
[7] A. Anani, A. Visintin, K. Petrov, S. Srinivasan, J.J. Reilly, J.R. Johnson, R.B. Schwarz, P.B. Desch, Alloys for hydrogen storage in nickel/hydrogen and nickel/metal hydride batteries, J. Power Sources 47 (1994) 261–275.
[8] K.-H. Young, J. Nei, C. Wan, R. Denys, V. Yartys, Comparison of C14- and C15-predomiated AB_2 metal hydride alloys for electrochemical applications,

Batteries 3 (2017) 22.
[9] Y. Liu, H. Pan, M. Gao, Q. Wang, Advanced hydrogen storage alloys for Ni/MH rechargeable batteries, J. Mater. Chem. 21 (2011) 4743–4755.
[10] K.-H. Young, J.M. Koch, C. Wan, R.V. Denys, V.A. Yartys, Cell performance comparison between C14-and C15-predomiated AB_2 metal hydride alloys, Batteries 3 (2017) 29.
[11] K.-H. Young, S. Chang, X. Lin, C14 Laves phase metal hydride alloys for Ni/MH batteries applications, Batteries 3 (2017) 27.
[12] D.-M. Kim, K.-J. Jang, J.-Y. Lee, A review on the development of AB_2-type Zr-based Laves phase hydrogen storage alloys for Ni–MH rechargeable batteries in the Korea Advanced Institute of Science and Technology, J. Alloy. Comp. 293 (1999) 583–592.
[13] F. Cuevas, J.-M. Joubert, M. Latroche, A. Percheron-Guégan, Intermetallic compounds as negative electrodes of Ni/MH batteries, Appl. Phys. A 72 (2001) 225–238.
[14] Y. Zhang, J. Li, T. Zhang, H. Kou, R. Hu, X. Xue, Hydrogen storage properties of non-stoichiometric $Zr_{0.9}Ti_xV_2$ melt-spun ribbons, Energy 114 (2016) 1147–1154.
[15] K. Young, T. Ouchi, J. Yang, M.A. Fetcenko, Studies of off-stoichiometric AB_2 metal hydride alloy: Part 1. Structural characteristics, Int. J. Hydrogen Energy 36 (2011) 11137–11145.
[16] S. Gorsse, D.B. Miracle, O.N. Senkov, Mapping the world of complex concentrated alloys, Acta Mater. 135 (2017) 177–187.
[17] S. Gorsse, F. Tancret, Current and emerging practices of CALPHAD toward the development of high entropy alloys and complex concentrated alloys, J. Mater. Res. 33 (2018) 2899–2923.
[18] M.C. Gao, D.B. Miracle, D. Maurice, X. Yan, Y. Zhang, J.A. Hawk, High-entropy functional materials, J. Mater. Res. 33 (2018) 3138–3155.
[19] A.A. Volodin, R.V. Denys, C. Wan, I.D. Wijayanti, B.P. Tarasov, V.E. Antonov, V.A. Yartys, Study of hydrogen storage and electrochemical properties of AB_2-type $Ti_{0.15}Zr_{0.85}La_{0.03}Ni_{1.2}Mn_{0.7}V_{0.12}Fe_{0.12}$ alloy, J. Alloy. Comp. 793 (2019) 564–575.
[20] C. Wan, R. Denys, M. Lelis, D. Milčius, V. Yartys, Electrochemical studies and phase-structural characterization of a high-capacity La-doped AB_2 Laves type alloy and its hydride, J. Power Sources 418 (2019) 193–201.
[21] M. Fichtner, Properties of nanoscale metal hydrides, Nanotechnology 20 (2009) 204009.
[22] C. Liu, F. Li, L.-P. Ma, H.-M. Cheng, Advanced materials for energy storage, Adv. Mater. 22 (2010) E28–E62.
[23] S. Suwarno, J.K. Solberg, J.P. Maehlen, B. Krogh, B.T. BØRresen, E. Ochoa-Fernandez, E. Rytter, M. Williams, R. Denys, V.A. Yartys, Microstructure and hydrogen storage properties of as-cast and rapidly solidified Ti-rich Ti–V alloys, Trans. Nonferrous Metals Soc. China 22 (2012) 1831–1838.
[24] S. Suwarno, J.K. Solberg, V.A. Yartys, B. Krogh, Hydrogenation and microstructural study of melt-spun $Ti_{0.8}V_{0.2}$, J. Alloy. Comp. 509 (2011) S775–S778.
[25] I.D. Wijayanti, L. Mølmen, R.V. Denys, J. Nei, S. Gorsse, K. Young, M.N. Guzik, V. Yartys, The electrochemical performance of melt-spun C14-Laves type TiZr-based alloy, Int. J. Hydrogen Energy (2019). https://doi.org/10.1016/j.ijhydene.2019.02.093.
[26] S.K. Zhang, K.Y. Shu, Y.Q. Lei, G.L. Lü, Q.D. Wang, Effect of solidification rate on the phase structure and electrochemical properties of alloy $Zr_{0.7}Ti_{0.3}(MnVNi)_2$, J. Alloy. Comp. 352 (2003) 158–162.
[27] Y. Wu, M.V. Lototskyy, J.K. Solberg, V.A. Yartys, Effect of microstructure on the phase composition and hydrogen absorption-desorption behaviour of melt-spun Mg-20Ni-8Mm alloys, Int. J. Hydrogen Energy 37 (2012) 1495–1508.
[28] A.C. Larson, R. Von Dreele, General Structure Analysis System (GSAS)(Report LAUR 86-748), Los Alamos, New Mexico, Los Alamos National Laboratory, 2004.
[29] X. Yuan, N. Xu, Comparative study on electrochemical techniques for determination of hydrogen diffusion coefficients in metal hydride electrodes, J. Appl. Electrochem. 31 (2001) 1033–1039.
[30] X. Yuan, N. Xu, Determination of hydrogen diffusion coefficient in metal hydride electrode by modified Warburg impedance, J. Alloy. Comp. 329 (2001) 115–120.
[31] S. Malifarge, B. Delobel, C. Delacourt, Determination of tortuosity using impedance spectra analysis of symmetric cell, J. Electrochem. Soc. 164 (2017) E3329–E3334.
[32] P. De Vidts, J. Delgado, R.E. White, Mathematical modeling for the discharge of a metal hydride electrode, J. Electrochem. Soc. 142 (1995) 4006–4013.
[33] K. Young, T. Ouchi, J. Koch, M.A. Fetcenko, The role of Mn in C14 Laves phase multi-component alloys for NiMH battery application, J. Alloy. Comp. 477 (2009) 749–758.
[34] K. Shu, S. Zhang, Y. Lei, G. Lü, Q. Wang, Effect of Ti on the structure and electrochemical performance of Zr-based AB_2 alloys for nickel–metal rechargeable batteries, J. Alloy. Comp. 349 (2003) 237–241.
[35] F. Stein, M. Palm, G. Sauthoff, Structure and stability of Laves phases part II—structure type variations in binary and ternary systems, Intermetallics 13 (2005) 1056–1074.
[36] K. Young, D.F. Wong, T. Ouchi, B. Huang, B. Reichman, Effects of La-addition to the structure, hydrogen storage, and electrochemical properties of C14 metal hydride alloys, Electrochim. Acta 174 (2015) 815–825.
[37] K. Young, B. Chao, D. Pawlik, H. Shen, Transmission electron microscope studies in the surface oxide on the La-containing AB_2 metal hydride alloy, J. Alloy. Comp. 672 (2016) 356–365.
[38] S. Kanazawa, Y. Kaneno, H. Inoue, W.Y. Kim, T. Takasugi, Microstructures and defect structures in $ZrCr_2$ Laves phase based intermetallic compounds, Intermetallics 10 (2002) 783–792.
[39] Y. Liu, K.-H. Young, Microstructure investigation on metal hydride alloys by electron backscatter diffraction technique, Batteries 2 (2016) 26.
[40] W. Lv, Y. Wu, Effect of melt spinning on the structural and low temperature electrochemical characteristics of La-Mg-Ni based $La_{0.65}Ce_{0.1}Mg_{0.25}Ni_3Co_{0.5}$ hydrogen storage alloy, J. Alloy. Comp. 789 (2019) 547–557.
[41] C.C. Nwakwuo, T. Holm, R.V. Denys, W. Hu, J.P. Maehlen, J.K. Solberg, V.A. Yartys, Effect of magnesium content and quenching rate on the phase structure and composition of rapidly solidified La_2MgNi_9 metal hydride battery electrode alloy, J. Alloy. Comp. 555 (2013) 201–208.
[42] R. Li, J. Wu, H. Su, S. Zhou, Microstructure and electrochemical performance of vanadium-containing AB_5-type low-Co intermetallic hydrides, J. Alloy. Comp. 421 (2006) 258–267.
[43] S.K. Zhang, Q.D. Wang, Y.Q. Lei, G.L. Lü, L.X. Chen, F. Wu, The phase structure and electrochemical properties of the melt-spun alloy $Zr_{0.7}Ti_{0.3}Mn_{0.4}V_{0.4}Ni_{1.2}$, J. Alloy. Comp. 330 (2002) 855–860.